A multiwavelength look at the GJ 9827 system: No evidence of extended atmospheres in GJ 9827b and d from HST and CARMENES data

(Article begins on next page)

18 October 2024

A multi-wavelength look at the GJ 9827 system
No evidence of extended atmospheres in GJ 9827 b and d from *HST* and CARMENES data

ILARIA CARLEO [1,2] ALLISON YOUNGBLOOD [3] SETH REDFIELD [1] NURIA CASASAYAS BARRIS [4,5] THOMAS R. AYRES [6] HUNTER VANNIER [1]
LUCA FOSSATI [7] ENRIC PALLE [4,5] JOHN H. LIVINGSTON [8] ANTONINO F. LANZA [9] PRAJWAL NIRAULA [10] JULIÁN D. ALVARADO-GÓMEZ [11]
GUO CHEN [12] DAVIDE GANDOLFI [13] EIKE W. GUENTHER [14] JEFFREY L. LINSKY [15] EVANGELOS NAGEL [14,16] NORIO NARITA [8,4,17,18,19]
LISA NORTMANN [4,20] EVGENYA L. SHKOLNIK [21] AND MONIKA STANGRET [4,5]

[1]*Astronomy Department and Van Vleck Observatory, Wesleyan University, Middletown, CT 06459, USA*
[2]*INAF – Osservatorio Astronomico di Padova, Vicolo dell'Osservatorio 5, I-35122, Padova, Italy*
[3]*Laboratory for Atmospheric and Space Physics, University of Colorado, Boulder, CO 80303, USA*
[4]*Instituto de Astrofísica de Canarias, C/Vía Láctea s/n, 38205 La Laguna, Spain*
[5]*Departamento de Astrofísica, Universidad de La Laguna, 38206 La Laguna, Spain*
[6]*Center for Astrophysics and Space Astronomy, University of Colorado, Boulder, CO 80309*
[7]*Space Research Institute, Austrian Academy of Sciences, Schmiedlstrasse 6, A-8041 Graz, Austria*
[8]*Department of Astronomy, University of Tokyo, 7-3-1 Hongo, Bunkyo-ku, Tokyo 113-0033, Japan*
[9]*INAF - Osservatorio Astrofisico di Catania, Via S. Sofia 78, I-95123, Catania, Italy*
[10]*Department of Earth, Atmospheric and Planetary Sciences, Massachusetts Institute of Technology, Cambridge, MA 02139*
[11]*Leibniz Institute for Astrophysics Potsdam An der Sternwarte 16, 14482 Potsdam, Germany*
[12]*Key Laboratory of Planetary Sciences, Purple Mountain Observatory, Chinese Academy of Sciences, Nanjing 210023, PR China*
[13]*Dipartimento di Fisica, Università degli Studi di Torino, via Pietro Giuria 1, I-10125, Torino, Italy*
[14]*Thüringer Landessternwarte Tautenburg, Sternwarte 5, D-07778 Tautenburg, Germany*
[15]*JILA, University of Colorado and NIST, Boulder, CO 80309-0440, USA*
[16]*Hamburger Sternwarte, Gojenbergsweg 112, D-21029 Hamburg, Germany*
[17]*Astrobiology Center, NINS, 2-21-1 Osawa, Mitaka, Tokyo 181-8588, Japan*
[18]*National Astronomical Observatory of Japan, NINS, 2-21-1 Osawa, Mitaka, Tokyo 181-8588, Japan*
[19]*JST, PRESTO, 7-3-1 Hongo, Bunkyo-ku, Tokyo 113-0033, Japan*
[20]*Institut für Astrophysik, Friedrich-Hund-Platz 1, D-37077 Göttingen, Germany*
[21]*School of Earth and Space Exploration Arizona State University, 781 S Terrace Road, Tempe, AZ 85281, USA*

ABSTRACT

GJ 9827 is a bright star hosting a planetary system with three transiting planets. As a multi-planet system with planets that sprawl within the boundaries of the radius gap between terrestrial and gaseous planets, GJ 9827 is an optimal target to study the evolution of the atmospheres of close-in planets with a common evolutionary history and their dependence from stellar irradiation. Here, we report on the *Hubble Space Telescope (HST)* and CARMENES transit observations of GJ 9827 planets b and d. We performed a stellar and interstellar medium characterization from the ultraviolet *HST* spectra, obtaining fluxes for Lyα and MgII of $F(\mathrm{Ly}\alpha) = (5.42^{+0.96}_{-0.75}) \times 10^{-13}$ erg cm^{-2} s^{-1} and $F(\mathrm{MgII}) = (5.64 \pm 0.24) \times 10^{-14}$ erg cm^{-2} s^{-1}. We also investigated a possible absorption signature in Lyα in the atmosphere of GJ 9827 b during a transit event from *HST* spectra, as well as Hα and He I signature for the atmosphere of GJ 9827 b and d from CARMENES spectra. We found no evidence of an extended atmosphere in either of the planets. This result is also supported by our analytical estimations of mass-loss based on the measured radiation fields for all the three planets of this system, which led to a mass-loss rate of 0.4, 0.3, and 0.1 planetary masses per Gyr, for GJ 9827 b, c, and d respectively. These values indicate that

Corresponding author: Ilaria Carleo
icarleo@wesleyan.edu

the planets could have lost their volatiles quickly in their evolution and probably do not retain an atmosphere at the current stage.

1. INTRODUCTION

The *Kepler* mission (Borucki et al. 2010) discovered that planets between the size of Earth and Neptune are the most common type of exoplanets in our Galaxy (i.e., Borucki et al. 2011; Batalha et al. 2013; Rowe et al. 2015). Defined as planets with radii between 1 and 4 $R_\oplus$, they do not have any analogue in our Solar System. This makes them very captivating targets for the study of their formation and evolution history, as well as understanding their compositions, interior structures, and atmospheres. Moreover, terrestrial planets may be the most attractive targets for the search of biosignatures.

One of the most interesting and still unexplained characteristics of the sub-Neptune sized planet population is the gap in the radius distribution around 1.6 $R_\oplus$ found by Fulton et al. (2017). Planet below this radius may be naked rocky cores, while those above this value have retained their atmospheres. A possible explanation for this gap suggests that gas-rich super Earths (mainly solid, rocky planets with a radius up to 1.5 $R_\oplus$) will retain or lose their envelope depending on the level of irradiation from their host stars (Lopez et al. 2012; Owen & Wu 2017; Loyd et al. 2020). It might be also possible that the mass-loss can be caused by the luminosity of the cooling planetary cores (core-powered mass-loss mechanism, Gupta & Schlichting 2019). In this context, observing small planets is essential to better understand the role of photo-evaporation in their evolution. Moreover, observing multi-planet systems offer an extra benefit, since such systems presumably formed under the same initial conditions (i.e., same age, same flux evolution) and provide a unique opportunity to compare the compositions of planets with different sizes, as well as atmospheric characteristics at different incident flux.

In this paper, we present the case of GJ 9827, a K6V star discovered to host three transiting planets in 1:3:5 commensurability by Kepler/K2 (Niraula et al. 2017; Rodriguez et al. 2018). Teske et al. (2018) showed with archival radial velocity (RV) observations from the *Magellan* II Planet Finder Spectrograph (PFS) that planet b has a mass of $\sim 8 \pm 2\, M_\oplus$, classifying it as one of the densest planets with an iron mass fraction of $\gtrsim 50\%$; while planets c and d did not show strong constraints on their masses. Prieto-Arranz et al. (2018) refined the planetary parameters through FIES, HARPS, and HARPS-N RVs, finding that planet b is less dense than suggested by Teske et al. (2018), with a mass of 3.74 ± 0.49 $M_\oplus$. Prieto-Arranz et al. (2018) also calculated the incident fluxes for the three planets, pointing to a rocky composition

for planets b and c, and a gaseous composition for planet d, which could possibly retain an extended atmosphere.

Rice et al. (2019) combined data from Niraula et al. (2017), Teske et al. (2018), Prieto-Arranz et al. (2018), and a new HARPS-N RV dataset, more precisely constraining the planetary masses for GJ 9827 b and d. A more recent analysis by Kosiarek et al. (2020) refined the ephemerides from *Spitzer* observations and, adding all the RVs from the previous work to their multi-year HIRES RV follow-up, more precisely constrained the parameters of this multi-planet system. The orbital periods, masses and radii of the three planets by (Kosiarek et al. 2020) are reported in Table 1 and are the ones used in our analyses. It is worth to notice that the radii of the three planets span the above-mentioned radius gap at ~1.6 $R_\oplus$, making this system even more appealing for uncovering how super-Earths form and evolve. Straddling this rocky/gaseous planets divide, GJ 9827 is ideal for studying the simultaneous evolution of planets at different orbital distances, having the stellar properties, including age, controlled.

A key aspect for the assessment of long-term habitability in a planetary system is the atmospheric mass loss of planets due to the high-energy environment and stellar wind of its host star. Several spectral lines sensitive to extended atmospheres have provided unique measurements of mass loss, including Lyman-α (e.g., Vidal-Madjar et al. 2003; Kulow et al. 2014; Ehrenreich et al. 2015), Hα (e.g., Jensen et al. 2012; Cauley et al. 2015; Casasayas-Barris et al. 2018), and He I 10830 Å (e.g., Spake et al. 2018; Salz et al. 2018; Nortmann et al. 2018; Allart et al. 2018). The far and extreme ultraviolet radiation from the star is capable of heating the upper portions of hot planet atmospheres, causing atoms to escape and possibly driving atmospheric mass loss (e.g., Murray-Clay et al. 2009; France et al. 2016; Linsky et al. 2020). This can have serious consequences for the evolution of the planet; if the mass-loss rate is high enough, the entire atmosphere can escape leaving behind a bare rocky core (e.g., Baraffe et al. 2005). This is especially relevant for planets with masses < 0.1 M_J, i.e., the Neptune and super-Earth regime (Owen & Wu 2013). Even in a less catastrophic case, the atmospheric composition of the planet can be highly altered (Lopez et al. 2012).

The photochemistry of planetary atmospheres hosted by cool stars is controlled by the two strongest UV emission lines in the stellar spectrum, Lyman-α (Lyα) and Mg II (Madhusudhan 2019). They can drive significant water loss (e.g.,

Luger et al. 2015; Miguel et al. 2015) and cause abiotic sources of biosignature gases (e.g., Tian et al. 2014; Harman et al. 2015). However, even for the nearest stars, absorption from the local interstellar medium (LISM) dramatically removes Lyα photons from the line of sight (Wood et al. 2005; Youngblood et al. 2016). The LISM is a rich and complex collection of clouds that leads to a unique absorption profile, often with more than one absorbing cloud (Redfield & Linsky 2004, 2008). To aid in the reconstruction of the intrinsic stellar Lyα flux, we observed and characterized the Mg II stellar emission, which samples a similar level of the stellar chromosphere as Lyα, and yet is significantly less altered by LISM absorption. Given then high column density for HI ($\log N \sim 18$ cm^{-2}), >70% of the intrinsic stellar chromospheric emission HI line can be absorbed by the LISM, and in some cases it can be >90% (Wood et al. 2005), whereas the lower abundances and column densities for MgII ($\log N \sim 12$ cm^{-2}), mean that <20% of the intrinsic stellar chromospheric emission MgII line is absorbed (Redfield & Linsky 2002). Fitting the MgII lines provides not only a characterization of the intrinsic chromospheric line shape for Lyα, but also a fit to the LISM absorption profile. Although Wood et al. (2005) used the line shape of MgII to inform the line shape of Lyα, the simultaneous fitting of the Lyα, MgII and ISM absorption that we perform in our analysis is novel.

We present here *HST* and CARMENES transit observations aimed at characterizing the atmosphere of GJ 9827 b, in particular to evaluate its transit signature in different wavelength domains. The CARMENES analysis also includes data for GJ 9827 d, the only planet of this system with previous atmospheric characterization: Kasper et al. (2020) investigated the 10,830 Å HeI triplet spectra, finding no absorption feature. In Section 2 we describe the observations and data reduction for *HST* and CARMENES data. We also used *HST* data for characterizing the star, with Lyα, MgII, and XUV fluxes estimation in Section 3. We investigate the possibility of an atmospheric planetary signal in Section 4 and finally present our discussion in Section 5 and conclusion in Section 6.

2. OBSERVATIONS AND DATA REDUCTION

2.1. *HST data*

A four-orbit *HST* pointing on GJ 9827 was carried out with the Space Telescope Imaging Spectrograph (STIS) during the 28 August 2018 transit of planet b as part of the Cycle 25 program GO-15434 (PI: S. Redfield). The first-order far-ultraviolet (FUV) grating G140M was used, with its 1222 Å setting, covering the wavelength interval 1194–1250 Å, at a resolution of $R \equiv \lambda/\Delta\lambda \sim 10^4$. The chromospheric H I 1215 Å Lyα line is formed in the range 1-3×10^4 K. Other important emission lines in this region are the Si III 1206 Å

resonance transition ($T \sim 5 \times 10^4$ K) and the N V 1240 Å doublet ($T \sim 2 \times 10^5$ K), although both of these were expected to be too faint to be significantly detected in the relatively brief FUV exposures of this faint, 10th-magnitude mid-K-type star. Nevertheless, the peak signal-to-noise (S/N) per 2-pixel resolution element (resel) in the combined spectrum at Lyα was about 35. The 52″×0.1″ narrow long slit was chosen to minimize geocoronal Lyα contamination from the upper atmosphere of the Earth. After the guide stars were acquired, a peak-up was performed to center GJ 9827, using the 31″×0.5″ NDC long slit in the visible at low resolution with the STIS CCD. The rest of the initial orbit was occupied by the first G140M exposure, of 1.8 ks. The remaining three orbits had single G140M exposures, of 2.9 ks each. A summary of the four FUV observations is provided in Table 2. In relation to the planetary transit, the first two exposures were pre-ingress, the third was in-transit, while the final was post-egress.

Three months later, a single-orbit out-of-transit near-ultraviolet (NUV) spectrum of the Mg II 2800 Å region of GJ 9827 was taken, again with STIS, but now using the high-resolution echelle E230H with its setting 2713 Å (2574–2851 Å) and the "spectroscopic" slit 0.2″×0.09″ to achieve optimum resolution ($R\sim110,000$) for the narrow Mg II absorptions. The 2713 Å setting also captures an important Fe II multiplet near 2600 Å, although unfortunately the NUV continuum of the mid-K star was too weak for the Fe II interstellar absorption to be detected (the peak S/N per resel at Mg II 2796 Å in the 1.8 ks exposure is 8). A visible-light peak-up was performed with the same slit prior to the E230H echelle exposure. The NUV observation is also described in Table 2.

We performed reductions of the FUV G140M exposures utilizing the pipeline-processed (CALSTIS) X2D files, which are wavelength- and flux-calibrated spatial/spectral images derived from rectified versions of the original long-slit stigmatic spectrograms. The image *x*-direction is along the dispersion, with 0.053 Å pixel^{-1}. The image *y*-direction is the spatial (cross-dispersion) dimension, with 0.03″ pixel^{-1}. The image pixel flux densities tabulated in the X2D files, and associated photometric errors, are provided per Å and per 0.0293″ (the latter is the cross-dispersion angular pixel size), so the extracted spectrum (and photometric error) must be multiplied by that angular factor to yield flux densities (erg cm^{-2} s^{-1} Å^{-1}).

The upper panel of Fig. 1 illustrates a co-added version of the 2D spatial/spectral image of the four G140M exposures. The vertical extent of the image represents a ±40 pixel slice in the detector *y*-direction ($\sim \pm1.2″$) centered on the apparent stellar Lyα feature. The horizontal extent is 1200 pixels along the dispersion. The narrow geocoronal stripe is conspicuous in the *y*-direction, bisecting the broader stellar Lyα

Table 1. Summary of GJ 9827 planets' parameters by Kosiarek et al. (2020) adopted for our analyses.

Planet	Orbital Period	Mass	Radius
	(days)	$(M_\oplus)$	$(R_\oplus)$
b	$1.2089765 \pm 2.3\times10^{-6}$	4.87 ± 0.37	1.529 ± 0.058
c	$3.648095 \pm 2.4\times10^{-5}$	1.92 ± 0.49	1.201 ± 0.046
d	$6.20183 \pm 1\times10^{-5}$	3.42 ± 0.62	1.955 ± 0.075

Table 2. Summary of *HST*/STIS exposures of GJ 9827.

Dataset	Mode-CENWAVE	Slit	UT Start Time	Exposure Time	Peak S/N [λ]
	(Å)	($''\times''$)	(yy–mm–dd.ddd)	(ks)	(resel^{-1} [Å])
ODRL01010	G140M–1222	52×0.1	2018–08–23.548	1.79	15 [1216.0]
ODRL01020	G140M–1222	52×0.1	2018–08–23.602	2.89	18 [1216.0]
ODRL01030	G140M–1222	52×0.1	2018–08–23.668	2.89	18 [1216.0]
ODRL01040	G140M–1222	52×0.1	2018–08–23.734	2.89	18 [1216.0]
ODRL03010	E230H–2713	0.2×0.09	2018–12–01.266	1.82	8 [2796.5]

feature. The red band outlines a 9-pixel flux extraction region (~0.3″) for the stellar spectrum, while the blue dashed bands highlight flanking regions where the background was sampled. The two background bands are 25 pixels wide, beginning at ±15 pixels from the center. The wide bands increase the signal-to-noise for the background subtraction. In practice, we eliminated the top three of the background values at each wavelength, in an effort to mitigate hot pixels.

The middle panel of Fig. 1 depicts the extracted 1D spectrum from the co-added image, zoomed into the Lyα feature. The green tracing is the gross spectrum; blue with grey shadow is the background including the geocoronal H I emission feature; and black is the net flux (gross–background). The wavelength scale was set to place the geocoronal Lyα feature at its laboratory wavelength (1215.670 Å). The thin red dashed curve represents the $10\,\sigma$ photometric error level (per resel), derived from the spatial/spectral values provided in the original X2D files, smoothed, for display, by a double pass of a rectangular filter 15 pixels wide. The bottom panel shows the extracted Lyα features for the four exposures separately, where the geocoronal feature has been subtracted from the stellar profile. There are small differences between the Lyα peaks of the four profiles, and the difference in the wing of the red profile (that corresponds to ODRL01010 of Table 2, the first observation of the sequence) around 1215 Å is close to 3σ in significance.

We reduced the single NUV exposure directly from the CALSTIS pipeline X1D file, which is a tabulation of extracted flux densities and associated photometric errors for 27 of the echelle orders contained in the original E230H-2713 spectral image. We merged the individual orders together, tapering the overlapping zones to preserve the optimum S/N. GJ 9827 is a relatively faint star for STIS high-resolution echelle spectroscopy, so the main features visible are the Mg II 2803 Å ("h") and 2796 Å ("k") resonance doublet, the most important spectral signatures of the stellar chromosphere below the temperatures where the higher-excitation Lyα emission forms. The peak S/N at the k line is about 8, and interstellar absorption is apparent in both emission cores.

The observed Lyα feature is the combination of the intrinsic stellar emission profile and the interstellar medium (ISM) attenuation profile (Wood et al. 2005). The core of the stellar emission line originates in the lower transition region and upper chromosphere ($T \sim 2$–3×10^4 K), while the outer wings form deeper in the stellar chromosphere. The Lyα emission core is strongly attenuated by neutral hydrogen (H I) and deuterium (D I) gas over the 29.7 pc sightline to GJ 9827. The star's +31.9 km s^{-1} radial velocity (Prieto-Arranz et al. 2018) shifts the stellar emission lines away from much of the ISM attenuation centered near 0 km s^{-1} (Redfield & Linsky 2008), giving the observed Lyα feature its asymmetric appearance. The Mg II cores are less affected than Lyα owing to the much smaller cosmic abundance of magnesium.
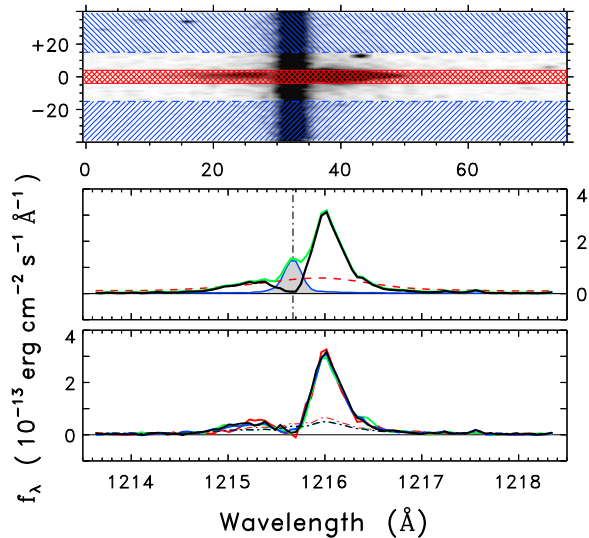
2.2. *CARMENES data*

Figure 1. *Top*: Co-added 2D spectral images (in pixels) of GJ 9827 G140M exposures. The red band represent flux extraction region for the stellar spectrum; the blue bands represent the region where the background, including geocoronal Ly-alpha, was sampled. *Middle*: Co-added 1D spectrum zoomed in the Lyα feature. The green curve is the total extracted spectrum; the gray shaded outlined by the blue curve is the background including the geocoronal emission; and black curve is the net flux (the total flux minus the background). The red dashed line is the photometric error. *Bottom*: Separate 1D spectra zoomed in the Lyα feature for the four exposures (ODRL01010 red, ODRL01020 green, ODRL01030 blue, ODRL01040 black). The thinner dotted-dashed curves are (smoothed) 3-sigma noise levels per resel for each of the spectra. The one for exposure 10 (in red) is higher than the others because the exposure was shorter.

We observed one transit of GJ 9827b and one transit of GJ 9827d with the CARMENES spectrograph (Calar Alto high-Resolution search for M dwarfs with Exo-earths with Near-infrared and optical Echelle Spectrographs; Quirrenbach et al. 2014, 2018) located at Calar Alto Observatory, in 13 August 2018 and 06 November 2018, respectively. CARMENES simultaneously covers the optical (VIS; 520 to 960 nm) and near-infrared range (NIR; 960 to 1710 nm), giving access to two important traces of planetary evaporation processes: the near-infrared He I triplet at 10830 Å and the visible Hα line at 6562.81 Å. GJ 9827 is sufficiently bright (V= 10.1 mag, J= 7.98 mag) to be observed with both arms simultaneously. Both observations were performed in stare mode, taking continuous exposures before, during, and after the transit. The exposure times were set to be nearly the same for both arms, so that accounting for the different readout overheads of the VIS and NIR arms, the central time of each exposure was coincident in both. Resetting of the Atmospheric Dispersion Corrector took place between two exposures (i.e. during readout) and approximately every 30 minutes.

For the planet b observations, the exposure time at the beginning was 190 s but was then increased to 198 s, and the averaged S/N achieved is 44 in the He I order and 30 in the Hα order. On the other hand, for the planet d observations, the exposure times were 200 s and 197 s, with a S/N of 47 and 35 around He I and Hα orders, respectively. Due to a cloud crossing, the exposures taken at 19:22, 19:26, and 19:30 UT presented S/N below 30 in the He I order and below 20 in the Hα order. These exposures are discarded from the atmospheric analysis. In addition, for technical reasons, the observations were stopped from 19:59 to 20:16 UT. We note strong telluric contamination of the He I region in both nights. A log table of the CARMENES observations is given in Table 3.

We reduced CARMENES observations with the CARMENES pipeline CARACAL (CARMENES Reduction And CALibration; Caballero et al. 2016), which performs bias, flat-relative optimal extraction (Zechmeister et al. 2014), cosmic-ray correction, and the wavelength calibration (Bauer et al. 2015). The wavelengths are given in vacuum and the reduced spectra referenced to the terrestrial rest frame.

3. STELLAR AND INTERSTELLAR MEDIUM CHARACTERIZATION

UV stellar emission dramatically affects the fate of an exoplanet's atmosphere, both in the physical and chemical composition and through possible mass loss, especially when the planet closely orbits its host star. EUV and X-ray photons heat an exoplanet's upper atmospheric layers and drive mass loss, whereas UV photons are primarily responsible for photochemistry (Madhusudhan 2019). In particular, the Lyα emission line at 1215.67 Å dominates the far ultraviolet (FUV) spectrum of late-type stars and is the main source for the photodissociation of molecules such as water and methane. However, the Lyα emission line is heavily absorbed by neutral hydrogen in the interstellar medium (ISM) between the star and the Earth and is also contaminated by the geocoronal emission. This necessitates a reconstruction to recover the intrinsic stellar flux as seen by the planet's atmosphere. In the next sections we describe the Lyα and Mg II emission line reconstructions for GJ 9827, the derived properties of the line-of-sight ISM, and how GJ 9827's UV emission compares to other K dwarfs.

3.1. *Intrinsic Lyman-α and Mg II reconstruction*

To correct for the ISM attenuation of the Lyα and Mg II lines and recover the intrinsic stellar emission lines, we use the approach described in Youngblood et al. (2016) and García Muñoz et al. (2020), modified to jointly fit Lyα and Mg II. This allows for stronger constraints on the physical

Table 3. Summary of CARMENES observations.

Observing night	2018–08–13	2018–11–06
Planet transit	GJ 9827 b	GJ 9827 d
Number of exposures VIS	43	40
Number of exposures NIR	43	39
Exposure time VIS (s)	200-192	200
Exposure time NIR (s)	190-198	197
Airmass change	1.86-1.28	1.51-1.27-1.31
Mean S/N in Hα order	30	35
Mean S/N in He I order	44	47

parameters common to the two transitions. Using a Markov Chain Monte Carlo method (Foreman-Mackey et al. 2013), we simultaneously fit a model of the Lyα and Mg II intrinsic stellar emission lines and ISM absorption lines to the STIS G140M and E230H spectra.

For Lyα, we parameterized the broad, intrinsic stellar emission line as a single Voigt profile in emission with a Gaussian in absorption for the line's self-reversal. For the narrow Mg II emission lines, we used a single Gaussian profile in emission for each line and a single Gaussian for each line's self-reversal. We required the radial velocities for the two Mg II lines to be identical and also required their FWHMs to be coupled such that $\text{FWHM}_k = 1.05 \times \text{FWHM}_h$, because high resolution stellar spectra indicate that the k line is ~5% broader than the h line (Brian E. Wood, private communication). We did not require the radial velocity of Lyα to match the Mg II lines in case of small wavelength offsets between the two gratings.

The ISM absorbers (H I, D I, Mg II) are modeled as single Voigt profiles in absorption (see Sec. 3.2 for justification for one component), each parameterized by a radial velocity v (offset from their corresponding stellar emission line's radial velocity), Doppler width b, and species column density N. We assume that the ISM absorbers are coming from the same interstellar gas with the same kinematics, so all three ISM species were required to have the same radial velocity offset from their stellar emission line's radial velocity, and the Doppler widths were all connected assuming pure thermal broadening by $b_{MgII} = b_{HI}/\sqrt{24.3}$ and $b_{DI} = b_{HI}/\sqrt{2}$. While H I and D I are dominated by thermal broadening and thus this assumption should be fine, but heavier species like Mg II will also have a significant contribution from turbulent broadening. Therefore, our value of b_{MgII} will underestimate

the true Doppler width of MgII. The D I and H I column densities were fixed to be $N(\text{D I})/N(\text{H I}) = 1.5 \times 10^{-5}$ (Wood et al. 2004), and $N(\text{Mg II})$ was not linked to $N(\text{D I})$ or $N(\text{H I})$. The corresponding intrinsic emission lines and ISM absorption lines were multiplied together and convolved to the corresponding instrument resolution using the STIS G140M and E230H line spread functions.

Given the lack of an in-transit detection (see Section 4.1), we co-added all four orbits' spectra to maximize the precision of the reconstruction. Figure 2 shows the best fit model and intrinsic profiles with 68% and 95% confidence intervals. We find an intrinsic Lyα flux with 68% confidence interval $(5.42^{+0.96}_{-0.75}) \times 10^{-13}$ erg cm^{-2} s^{-1}. For Mg II, we find a best-fit integrated flux of the h line of $(2.30 \pm 0.16) \times 10^{-14}$ erg cm^{-2} s^{-1}, and the integrated flux of the k line is $(3.34 \pm 0.17) \times 10^{-14}$ erg cm^{-2} s^{-1} (Figure 4). The total flux is F(Mg II h + k) = $(5.64 \pm 0.24) \times 10^{-14}$ erg cm^{-2} s^{-1}. These fluxes and the fitted ISM parameters (described in 3.2) are printed in Table 4.

In Figure 3, we compare the line core shapes of the reconstructed Lyα and Mg II lines, with ISM attenuation and instrument resolution effects removed. The Lyα line is >100 km s^{-1} broader than Mg II, as expected. Their self-reversal shapes are roughly similar, but there are significant discrepancies between the depth, width, and asymmetry of the two species. For Lyα, the self-reversal was only allowed to deviate ±10 km s^{-1} from line center due to significant degeneracy between the self-reversal depth and ISM absorption, but is centered almost exactly at line center. The self-reversal in the Mg II lines was allowed to vary more widely, and it is readily apparent from the observed spectra that the self-reversal is asymmetric (i.e., not centered exactly at the stellar velocity). The Lyα self-reversal depth also appears larger than Mg II's, however, the uncertainty on Lyα's self-reversal parame-

ters are extremely large as the line core is not observed due to severe ISM attenuation.

3.2. *Interstellar Medium Characterization*

We used the LISM Kinematic Calculator[1] (Redfield & Linsky 2008), which calculates whether or not a cloud of LISM traverses any given sight line, in addition to the radial and traverse velocities of the clouds in a given direction. In the case of GJ 9827, the LISM Kinematic Calculator yields no traversing clouds along the sight line. We note that this is likely due to the boundaries of clouds not being well sampled by limited LISM datasets, and this sight line probably does traverse at least one LISM cloud. There are 5 clouds passing within 20° of GJ 9827's sight line, including the Local Interstellar Cloud (LIC). The radial velocities of these clouds range from –7 to +10 km s^{-1} with a weighted average of –3.1±5.8 km s^{-1}. Given the limitations of our data (low S/N in Mg II and low spectral resolution for H I), we fit a single ISM cloud component to our spectra. This results in fitted parameters that are likely akin to an average of the true parameters of the multiple clouds along the sight line. From our reconstructions described in the previous section, we find for interstellar H I the following parameters: $v_{HI} = -3.35^{+2.81}_{-2.83}$ km s^{-1}, $\log_{10} N(\text{H I}) = 18.22^{+0.08}_{-0.10}$ cm^{-2}, and $b_{HI} = 12.8^{+2.2}_{-4.5}$ km s^{-1}. For interstellar Mg II, we find $\log_{10} N(\text{Mg II}) = 12.11^{+0.51}_{-0.59}$ cm^{-2}. Recall that Mg II's Doppler b parameter is defined as $b_{HI}/\sqrt{24.3}$ and the offset between the ISM radial velocity and the intrinsic stellar radial velocity was defined to be the same for the two species. This gives $v_{MgII} = 2.45^{+2.07}_{-2.31}$ km s^{-1} and $b_{MgII} = 2.6^{+0.4}_{-0.9}$ km s^{-1}. While we expect b_{MgII} to be underestimated, this is within the reasonable range for the Doppler width of LISM Mg II absorption (Redfield & Linsky 2004). Note that the absolute uncertainty in the STIS MAMA wavelength calibration is 0.5–1 pixels, or 6–12 km s^{-1} for G140M at Lyα and 1.5–3.0 km s^{-1} for E230H at Mg II.

The constraint on the Mg II interstellar absorbers is weak because of the narrowness of the stellar emission line serving as a backlight for the interstellar Mg II ions to absorb against. The interstellar Mg II atoms are Doppler shifted almost –30 km s^{-1} from an emission line with FWHM = 24 km s^{-1}, and no stellar continuum is detected around the stellar emission lines.

From our simultaneously-fitted H I and Mg II column densities, we calculate the ratio $N(\text{MgII})/N(\text{HI}) = 8.0^{+18.3}_{-6.0} \times 10^{-7}$ for GJ 9827's sight line. This value overlaps with the $N(\text{MgII})/N(\text{HI})$ ratio from Linsky (2019) (($3.6^{+2.8}_{-1.6}$) × 10^{-6}) at the 68% confidence interval (2.0×10^{-7}–2.6×10^{-6}).

To verify our measurement of the Mg II ISM absorption, we also applied the ISM fitting technique described in Redfield & Linsky (2002). We assume the interstellar absorbers have a radial velocity equal to the LIC for this line-of-sight (+1.24 km s^{-1}; Redfield & Linsky 2008), and we assume the wings of the Mg II emission line to be symmetric. Masking the blueward, ISM-affected half of the line, we mirrored the redward half of the Mg II k profile to create the assumed intrinsic stellar profile, which clearly indicated the presence of ISM absorption in the blue wing. The low S/N ratio in the wings of the line prevented a free fit to the column density. However, visual inspection using the mirrored profile led to a minimum column density $\log_{10} N(\text{Mg II}) \approx 12.5$. This value is 0.14 dex above the 1-σ uncertainty range of the previous fitting results shown in Figure 4. Using the $\log_{10} N(\text{Mg II})=12.5$ value from our mirrored profile fitting of the Mg II line, we find $N(\text{MgII})/N(\text{HI}) = 1.9 \times 10^{-6}$, which is in agreement with the ratio value from Linsky (2019). The conclusion from using two different methods is that LISM absorption is present on the blueward wing, although it does not significantly alter the Mg II emission profile. Our assumption of a single LISM absorption component and our choice of the stellar emission profile (i.e., automated Gaussian versus a mirrored profile) do not formally enter into our error analysis, and given the comparison to the LISM average $N(\text{MgII})/N(\text{HI})$ ratio indicate that our Mg II LISM column density may be slightly underestimated.

We also searched for other ISM-affected spectral lines in the spectral range of STIS/E230H (2576 - 2823 Å), such as the iron lines at 2586 and 2600 Å, but the S/N is too low and the spectrum does not present any other spectral features.

3.3. *GJ 9827 and other K dwarfs*

We compare GJ 9827's Lyα and Mg II fluxes to other K dwarfs with measured fluxes for both lines (Fig. 5). To compare to data from Wood et al. (2005) and Youngblood et al. (2016), we convert our fluxes into surface fluxes using the 0.579±0.018 R$_\odot$ radius from Kosiarek et al. 2020 and the 29.69 pc distance from Gaia DR2 to obtain $F_S(\text{Lyα}) = (2.81^{+0.50}_{-0.39}) \times 10^6$ erg cm^{-2} s^{-1} and $F_S(\text{MgII}) = (2.92\pm0.13) \times 10^5$ erg cm^{-2} s^{-1}. GJ 9827's rotation period is poorly constrained, but appears to be between 15-30 days with a most likely value of 28.72 days (Rice et al. 2019).

Compared to other K dwarfs of similar rotation period[2], GJ 9827 has approximately 3.0 times less Mg II surface flux, and 2.8 times more Lyα surface flux. Mg II is commonly used as an estimator for the difficult-to-observe Lyα

---

[2] The comparison K dwarfs with rotation period >15 days include HD 40307, HD 85512, HD 97658, α Cen B, 61 Cyg A, ε Ind, 40 Eri A, 36 Oph A, and σ Gem. More information on all the K dwarfs in Figure 5 can be found in Wood et al. (2005) and Youngblood et al. (2016).

---

[1] lism.wesleyan.edu/LISMdynamics.html

Table 4. Stellar and ISM parameters.

Parameter	Value	Units
Stellar fluxes		
Intrinsic Lyα flux F(Lyα)	$(5.42^{+0.96}_{-0.75}) \times 10^{-13}$	erg cm^{-2} s^{-1}
Intrinsic MgII h flux F(MgII h)	$(2.30 \pm 0.16) \times 10^{-14}$	erg cm^{-2} s^{-1}
Intrinsic MgII k flux F(MgII k)	$(3.34 \pm 0.17) \times 10^{-14}$	erg cm^{-2} s^{-1}
Intrinsic MgII $h + k$ flux F(MgII h+k)	$(5.64 \pm 0.24) \times 10^{-14}$	erg cm^{-2} s^{-1}
Surface Lyα flux F_S(Lyα)	$(2.81^{+0.50}_{-0.39}) \times 10^{6}$	erg cm^{-2} s^{-1}
Surface MgII flux F_S(MgII)	$(2.92 \pm 0.13) \times 10^{5}$	erg cm^{-2} s^{-1}
ISM absorbers' parameters		
HI radial velocity v_{HI}	$-3.4^{+2.8}_{-2.8}$	km s^{-1}
HI Doppler width b_{HI}	$12.8^{+2.2}_{-4.5}$	km s^{-1}
HI column density $\log_{10}N$(HI)	$18.22^{+0.08}_{-0.10}$	cm^{-2}
MgII radial velocity v_{MgII}	$2.5^{+2.1}_{-2.3}$	km s^{-1}
MgII Doppler width b_{MgII}	$2.6^{+0.4}_{-0.9}$	km s^{-1}
MgII column density $\log_{10}N$(MgII)	$12.11^{+0.51}_{-0.59}$	cm^{-2}
N(MgII)/N(HI)	$8.0^{+18.3}_{-6.0} \times 10^{-7}$	

Note—The stellar radial velocity is +31.9 km s^{-1} (Prieto-Arranz et al. 2018). The v_{HI} and v_{MgII} values are derived from the same free parameter in the fit, a radial velocity offset from the stellar H I and Mg II emission lines centroids. The v_{HI} and v_{MgII} values differ because of differences in the absolute wavelength solution between the two gratings (G140M and E230H). The b_{HI} and b_{MgII} values are also derived from the same free parameter (b_{HI}) under the assumption of thermal line broadening ($b_{MgII} = b_{HI}/\sqrt{24.3}$).

line (Wood et al. 2005), and if we relied on the Mg II observation to estimate GJ 9827's Lyα emission, we would have underpredicted it by almost a factor of 5. Figure 2 shows how this MgII-derived Lyα profile (both intrinsic and observed) would appear and how the Lyα spectrum strongly rules out this flux level at the $>3\sigma$ level. This underestimation could have significant consequences for the atmospheres of GJ 9827's planets, because Lyα has a strong effect on photochemistry and as a proxy for the EUV (Linsky et al. 2014), could have implications for the atmospheric escape from the planets.

We estimate that there is a 0.001% probability that GJ 9827's Lyα flux is consistent with the other K dwarfs in Figure 5, and a 16% probability that its Mg II flux is consistent with other K dwarfs. To calculate this, we drew 10^6 random samples from GJ 9827's Lyα and Mg II flux posterior distributions as well as 10^6 random samples from a normal distribution describing the red best-fit lines in the middle and right panels of Figure 5, and determined what percentage of the posterior samples overlapped with samples from the best-fit lines. The normal distributions describing the best-fit lines had means equal to zero, and standard deviations equal to the standard deviations of all data points about the best-fit line,

normalized by the best-fit line. For Lyα, the standard deviation is 0.29 and for Mg II it is 0.46. The samples from the Lyα and Mg II posterior distributions were also cast as differences from the best-fit line and then normalized by the best-fit line.

What is causing the apparently significant discrepancy in the Mg II - Lyα flux ratio for this star? It is possible that this ratio is within the expected scatter of K dwarf UV flux-flux relations, and more UV spectroscopic observations K dwarfs are needed to quantify that typical scatter. Mg II and Lyα form in slightly different regions in the stellar atmospheres and therefore their emission mechanisms are not exactly coupled, but in practice the scatter is likely dominated by the non-simultaneity of the Mg II and Lyα observations. For example, the GJ 9827 Mg II and Lyα observations were taken 100 days apart, or approximately 3.5 stellar rotation periods apart. Stellar surface inhomogeneities (e.g., active regions, faculae, plage) as well as evolution of these features responsible for much of the Mg II and Lyα emission could cause deviations in the expected Mg II - Lyα flux ratio.

Here we consider some additional effects, including metallicity and rotation evolution. GJ 9827 has slightly sub-solar metallicity ([M/H] = -0.26 to -0.5; Rice et al. 2019), which

could potentially explain a low Mg II flux relative to Lyα as well as GJ 9827's potentially anomalously-high Lyα flux. A detailed investigation into the effect of metallicity on relative Mg II and Lyα line strengths in K dwarfs would be needed to determine that. Another possible explanation is the observed rotation evolution of Lyα luminosity compared to less optically thick chromospheric lines like C II. Pineda et al. (*under review*) showed with a sample of young and field age M dwarfs that Lyα luminosity declines much more slowly with increasing stellar rotation period (a proxy for stellar age) than other far-UV lines like C II. Assuming that Mg II behaves more similarly to lines like C II rather than Lyα, GJ 9827 could be at a point in its rotational evolution when its Mg II luminosity has decreased significantly but Lyα has not been impacted as much by stellar spindown. More UV observations of low-activity K dwarfs are needed to determine if this increasing Lyα/Mg II flux ratio with increasing rotation period is a real effect.
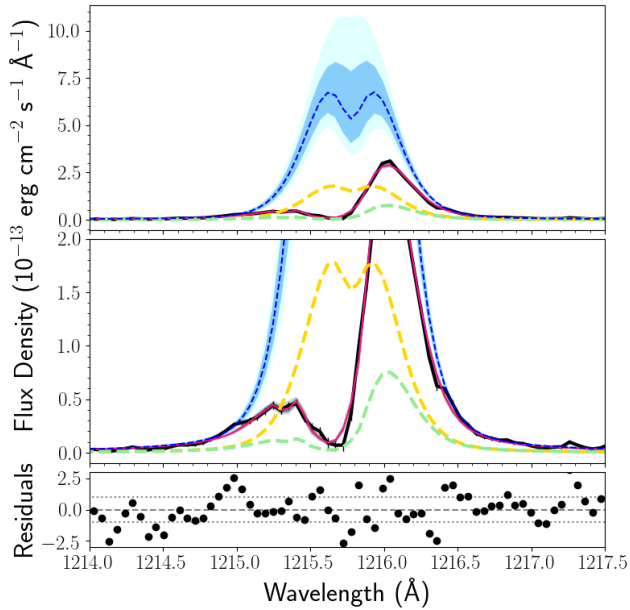

Figure 3. The intrinsic stellar profiles for Lyα and Mg II are shown here, with ISM attenuation and instrumental resolution effects removed. Only the Mg II k line is shown for visual clarity, but the h line appears very similar to the k line. The profiles have been normalized to their peak values, and 68% confidence intervals are shown as the shaded regions.

Figure 4. Reconstructed (orange dashed line) and fitted (attenuated; solid green line) Mg II profiles are shown. The ISM absorption is weak and centered at 2796.38 Å and 2803.56 Å; the effect on the resultant profile is small. In the left panel, the dotted green line shows the model of the attenuated profile with the 2-σ upper limit on the Mg II column density ($\log_{10} N$(Mg II) < 13.33). The bottom panels show the residuals (data-model)/(data uncertainty).

Figure 2. The reconstruction of the Lyα profile is shown in the top two panels (the middle panel is a zoomed version of the top panel with no changes). The STIS spectrum is represented in black with error bars (the error bars are generally smaller than the black line width). The best-fit model and 68% and 95% confidence intervals is shown as the pink line, dark gray shading, and light gray shading, respectively (the confidence intervals are also generally thinner than the width of the pink line). The intrinsic stellar emission line corresponding to the best-fit model is shown as the dashed blue line, with the 68% and 95% confidence intervals shown as dark-blue and light-blue shading, respectively. The bottom panel shows the residuals (data-model)/(data uncertainty). The dashed gold and green lines show how the intrinsic and observed (ISM attenuated) spectra would respectively appear if the intrinsic fluxes were consistent with Mg II - Lyα fluxes from the literature (Section 3.3).
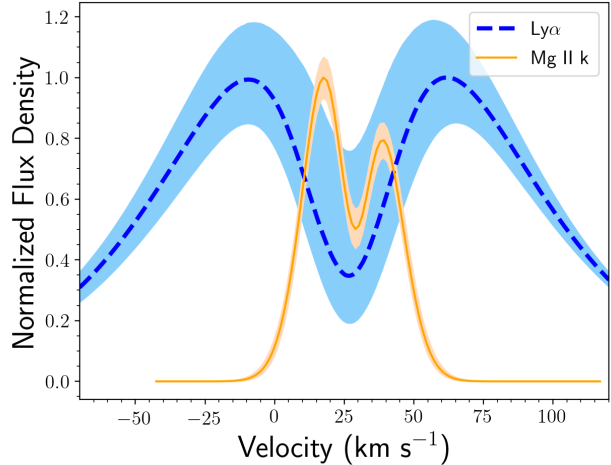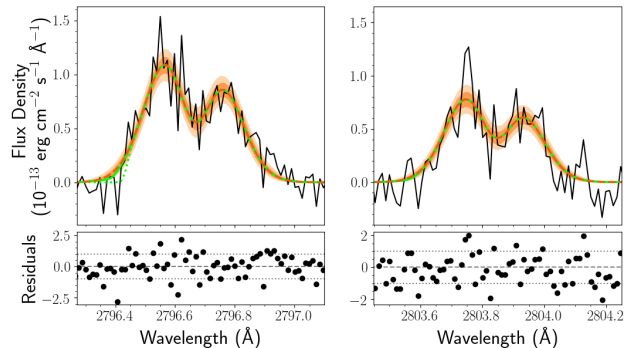
4. SEARCHING FOR PLANETARY ATMOSPHERIC ABSORPTION SIGNAL

4.1. *Investigating Lyman-α*

We investigate the behaviour of GJ 9827's observed Lyα profiles during the different phases of the transit. Starting from the four spectra obtained in Section 2.1 (one per orbit) we calculated the in-transit absorption depth as $1 - F_{IN}/F_{OUT}$, where F_{IN} is the flux of the Lyα line during the transit and F_{OUT} is the out-of-transit flux. Fig. 6 shows the out-of-transit (black solid line) and in-transit (red solid line) spectra for
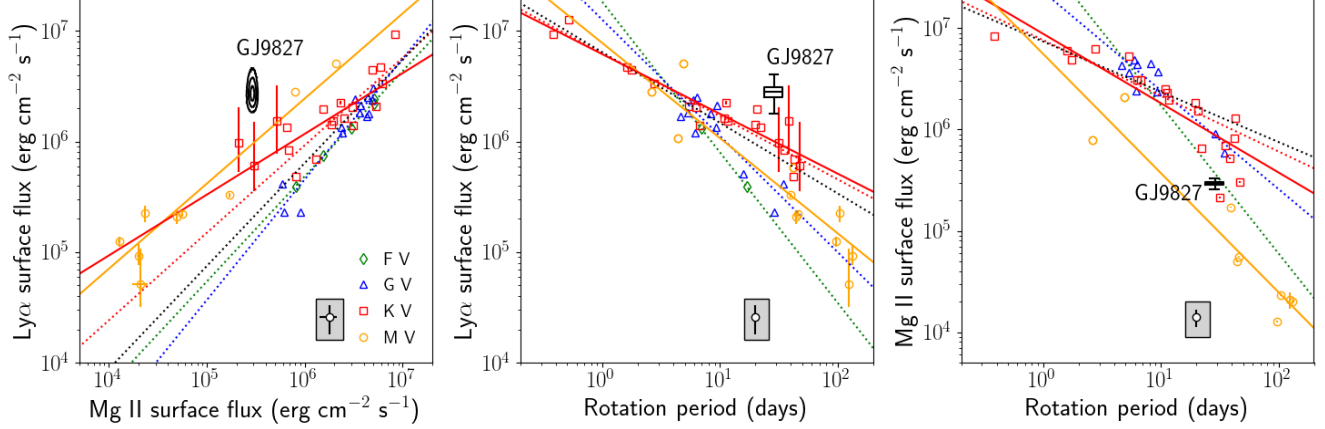
Figure 5. GJ 9827's Lyα and Mg II surface fluxes (corrected for ISM absorption) and rotation period are compared to other F, G, K, and M stars from the literature (Wood et al. 2005; Youngblood et al. 2016). The literature sample is shown in colored, open symbols with corresponding best-fit linear regressions (dashed lines from Wood et al. 2005, solid lines from Youngblood et al. 2016). The example error bars in each panel apply to colored symbols without error bars. In the left panel, the 68%, 95%, and 99.7% confidence intervals from our simultaneous Lyα and Mg II reconstruction are shown as black contours. In the right two panels, the black box and whisker symbol shows the median Lyα and Mg II surface flux with the 68% and 95% confidence intervals as the box and whiskers, respectively at the assumed stellar rotation period (28.72 days; Rice et al. 2019).

GJ 9827 b, where the out-of-transit spectrum (F_{OUT}) is obtained by averaging the three out-of-transit spectra and the single in-transit spectrum represents F_{IN}. We find that the observed Lyα spectra are very similar in and out of the transit, and there is no evident planetary absorption during the transit. The largest apparent absorption depths occur in the spectral region most strongly contaminated by ISM absorption and geocoronal emission.
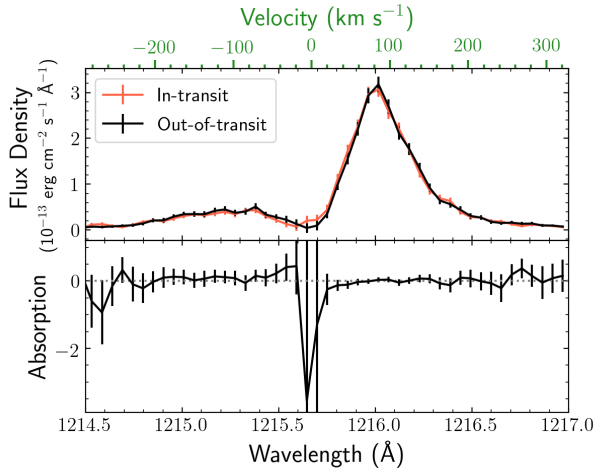
creating strong absorption signatures many hours before and after the optical transit. Fig. 7 shows pre-ingress and post-egress spectra in the top panel, and the difference between these spectra in the bottom panel. No evident difference is found.
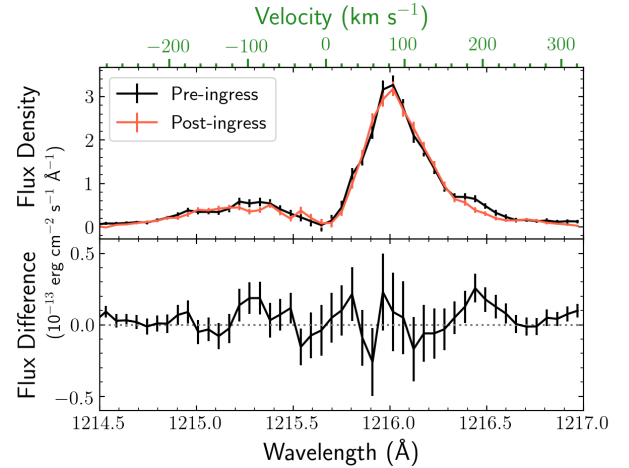

Figure 7. *Top.* Pre-ingress Lyα spectrum (black line) (black line) and post-egress Lyα spectrum (red line). *Bottom.* Difference between pre-ingress and post-egress spectra.

Figure 6. *Top.* Lyα line of GJ 9827 during the transit (red line) and outside (black line). *Bottom.* In-transit absorption depth, $1 - F_{\mathrm{IN}}/F_{\mathrm{OUT}}$.

Furthermore, we compare pre-ingress and post-egress spectra, as in Kulow et al. (2014), to search for a possible atmospheric comet-like tail. McCann et al. (2019) showed that the stellar wind can significantly shape the planetary outflow,

We integrated the flux in the Lyα blue wing from -250 to -75 km s^{-1} in the stellar rest frame (1214.787-1215.496 Å) to obtain the average fluxes of each of the four orbits (units 10^{-15} erg cm^{-2} s^{-1}): 2.20±0.19, 2.28±0.15, 2.16±0.15, and 2.41±0.16. To obtain an upper limit of the size of the planet's H I atmosphere, we fit a transit model of an opaque sphere using a MCMC routine. We use the batman package (Kreid-

berg 2015) with transit ephemerides from Rice et al. 2019 and uniform limb darkening parameters. The size of the planet at Lyα relative to the star ($R_{Ly\alpha}/R_\star$) was the only free parameter, and we find 1-σ, 2-σ, and 3-σ upper limits of 0.36, 0.48, and 0.57 for $R_{Ly\alpha}/R_\star$ in the blue wing. We repeated this upper limit calculation for the Lyα red wing (+10 to +250 km s^{-1} in the stellar rest frame; 1215.841-1216.813 Å) and find average fluxes of each of the four orbits (units 10^{-13} erg cm^{-2} s^{-1}) of 1.10±0.04, 1.10±0.03, 1.09±0.03, and 1.13±0.03. The 1-σ, 2-σ, and 3-σ upper limits on $R_{Ly\alpha}/R_\star$ in the red wing are 0.21, 0.27, and 0.32.

4.2. *Investigating He I and Hα*

Prieto-Arranz et al. (2018) suggested that the GJ 9827 planetary system is an excellent laboratory to test atmospheric evolution and planetary mass-loss rates. We investigate the presence of evaporation traces in the atmospheres of GJ 9827 b and GJ 9827 d using CARMENES observations. In particular, we use the data obtained with the near-infrared channel to study the He I triplet lines (at 10829.09 Å, 10830.25 Å and 10830.34 Å), and the visible channel data to study the Hα line (at 6562.81 Å).

As a first step, we correct the observed spectra of telluric absorption contamination using `molecfit` (Smette et al. 2015 and Kausch et al. 2015), assuming the parameters presented in Nagel et al. (submitted) for the CARMENES instrumental line spread function model. In particular, the He I region is contaminated by telluric absorption of water vapor and telluric emission of OH (Nortmann et al. 2018; Salz et al. 2018). The water vapour absorption is corrected with `molecfit` and the OH emission lines are masked, following the methods described in Palle et al. (2020). The telluric line removal and masked regions are illustrated for each planet/night in the top panels of Figures 8 and 9.

After removing the telluric contamination, we can extract the transmission spectrum in both He I and Hα regions using the same approach, presented in different studies such as Wyttenbach et al. (2015), Casasayas-Barris et al. (2019), and Chen et al. (2020). CARMENES observations are referenced to the Earth's rest frame. Thus, we shift the spectra to the stellar rest frame considering the barycentric radial velocity information and the system velocity (31.95 km s^{-1}; Prieto-Arranz et al. 2018). After computing the ratio of each stellar spectrum to the master out-of-transit spectrum (combination of all out-of-transit spectra using the simple average) we move the residuals to the planet rest frame (see middle panels of Figures 8 and 9). To do this, we calculate the planet's radial velocity using the radial velocity semi-amplitudes $K_p^{\rm b}$ = 166.3 km s^{-1} and $K_p^{\rm d}$ = 98.2 km s^{-1}, for GJ 9827 b and GJ 9827 d, respectively. These values are calculated assuming the stellar radial velocity semi-amplitude ($K_\star$), and the planet and star masses reported by Kosiarek

et al. (2020), and using $K_p = K_\star M_\star / M_p$ (Birkby 2018). Finally, we combine all in-transit residuals in the planet rest frame to obtain the transmission spectrum. In the He I region, the masked intervals due to OH contamination are the same for all spectra in the stellar rest frame, but change when moving the spectra to the planet rest frame. When combining the in-transit residuals to extract the transmission spectrum, we only include the non-masked pixels in the calculation. The final transmission spectra are presented in the bottom panels of Figures 8 and 9. We note that different $K_\star$ and mass values are reported in the literature, which result in different K_p values (see Rice et al. 2019 or Prieto-Arranz et al. 2018, for example). However, these different K_p values do not have significant impact on the derived transmission spectra.

It is important to notice, however, that using the parameters from Kosiarek et al. (2020), the mid-transit time of GJ 9827 d's observations differs from that obtained using the parameters from Prieto-Arranz et al. 2018, Rodriguez et al. 2018, and Rice et al. 2019. This difference is produced, mainly, by the differences in the derived orbital period value. The orbital period derived by Kosiarek et al. (2020) differs by more than 30 s from the ones presented in the previous studies, and this difference is propagated along the different epochs. To be on the safe side, we have repeated the analysis using the parameters from the different references and the resulting transmission spectra do not show any significant feature in any of the cases.

In the two-dimensional residual maps presented in Figures 8 and 9, we are not able to visually distinguish absorption features during the transit that could have planetary origin, for either of He I or Hα. The overall transmission spectrum does not show significant absorption features either. The excess absorption measured in the transmission spectra of GJ 9827 b using a 0.7 Å passband centred on the He I and Hα lines core is −0.3 ± 0.2 % and −0.2 ± 0.2 %, respectively. On the other hand, for GJ 9827 d, we measure +0.2 ± 0.2 % and −0.1 ± 0.2 % excess, respectively. The expected absorption signal ($\approx 2nHR_p/R_\star^2$) of the annular area of one ($n = 1$) atmospheric scale height (H) during the transit is around 3×10^{-5} for both planets, respectively, assuming an atmosphere dominated by H/He mixture and near solar composition ($\mu = 2.3$). However, it has been observed in several exoplanet observations that the detected He I signals are comparable to those created by an annular area of $n = 100$ times the scale height (see dos Santos et al. 2020). Here, with only a single transit per planet, and the relatively small S/N ratio of the observations, especially in the lines core, we find no evidence for an extended H/He upper atmosphere around GJ 9827 b or GJ 9827 d. This is consistent with the non-detection He I presented for GJ 9827 d by Kasper et al. (2020).
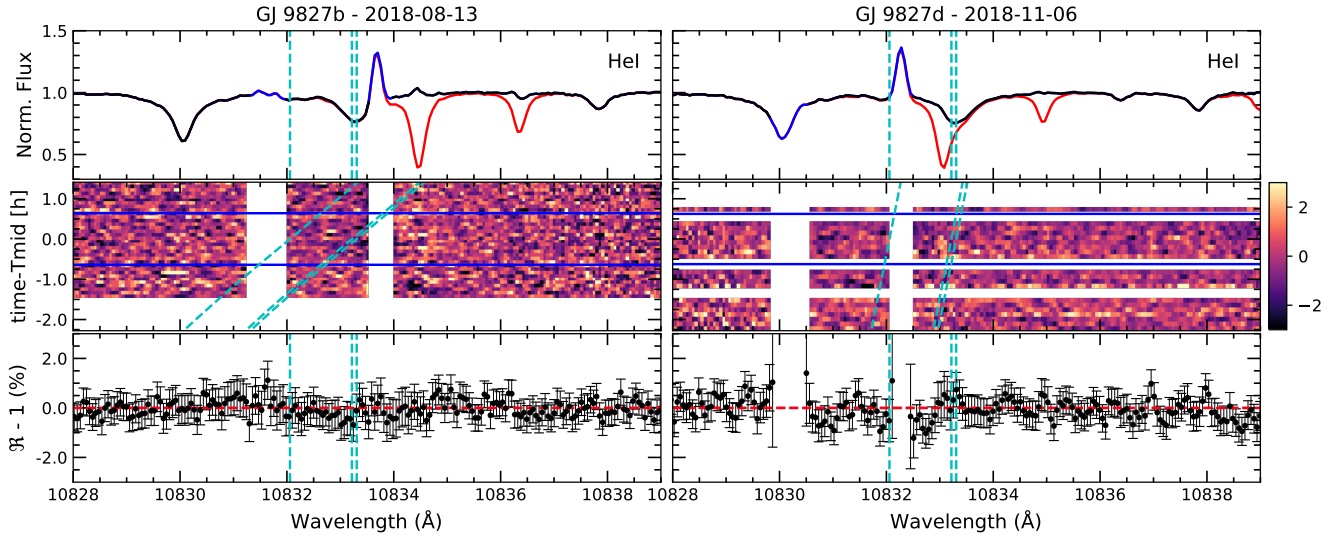
Figure 8. CARMENES transmission spectroscopy results around the near-infrared He I triplet for GJ 9827 b (left column) and GJ 9827 d (right column). Top panel: GJ 9827's spectra in the He I region. In the spectra we mark in red the telluric absorption lines and in blue the OH telluric emission lines region. In black we plot the spectra used to construct the transmission spectra, where the telluric absorption lines are corrected with Molecfit and the telluric OH emission lines are masked. The vertical/oblique cyan broken lines mark the positions of the triplet lines. Middle panel: 2D map of the residuals after dividing each spectrum by the master out-of-transit spectrum, in the stellar rest frame. The blue horizontal lines show the first and fourth contacts of the transit. The color scale shows the relative flux (F_{in}/F_{out} -1) in %. The white vertical regions correspond to the masked emission lines and the horizontal white regions to time stamps for which observations were discarded or missing. The vertical/oblique cyan broken lines mark the expected trace of the triplet lines during transit. The data are binned by 0.003 and 0.0008 in orbital phase for GJ 9827 b and GJ 9827 d, respectively. Bottom panel: The transmission spectrum for GJ 9827 b and GJ 9827 d. The red dashed line marks the zero absorption level. Again, the cyan dashed vertical lines show the position of the He I triplet lines. All wavelengths are presented in the vacuum.
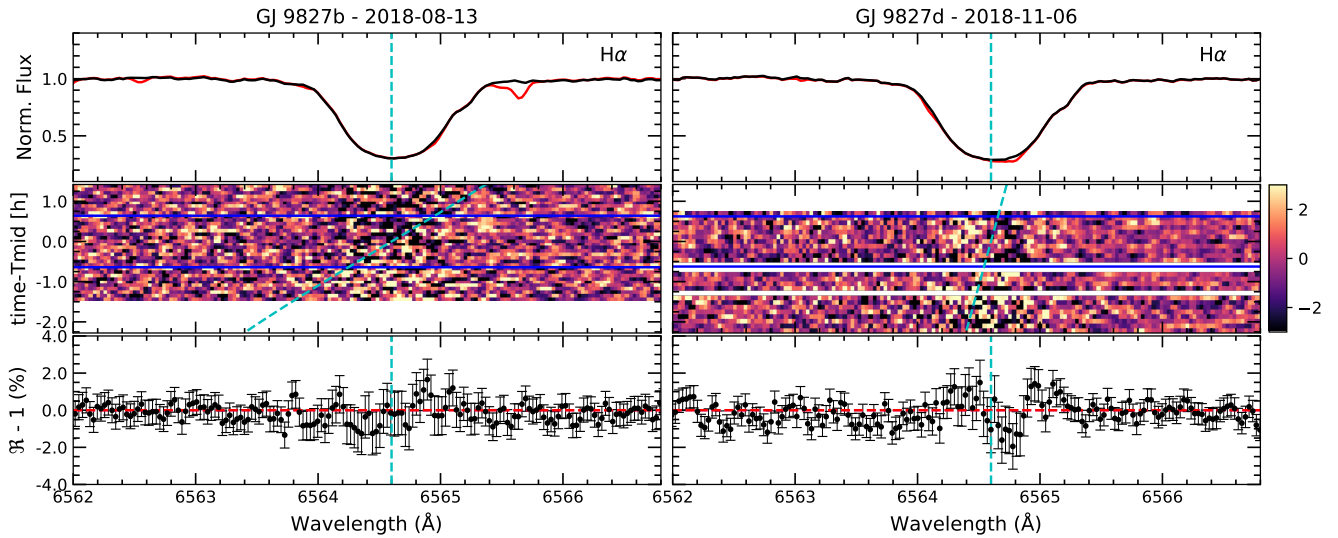

Figure 9. Same as Fig. 8 but around the Hα line. In this wavelength region only telluric absorption contamination is observed and no spectral regions are masked.

5. DISCUSSION

The non-detection of planetary Lyα absorption during the transit of GJ 9827 b can be the result of several factors. The particular radial velocity of the host star is such that the interstellar medium absorbs the line core and most of the blue wing of the Lyα line, while the red wing is almost intact. This is relevant, because past Lyα transit observations obtained for both hot Jupiters and warm Neptunes have shown that the planetary atmospheric absorption is strongest in the blue wing and it is typically caused by energetic neutral atoms, which are fast stellar wind protons that received electrons from slow planetary hydrogen atoms via charge exchange and are moving towards us at velocities of the order of $100\,\mathrm{km\,s^{-1}}$ (e.g., Vidal-Madjar et al. 2003; Kislyakova et al. 2014; Ehrenreich et al. 2015; Khodachenko et al. 2017; Shaikhislamov et al. 2020). Weak planetary atmospheric absorption in the red wing of the Lyα line, attributed to natural and thermal line broadening, has been observed before, for example in the case of HD209458b (Vidal-Madjar et al. 2003), but this absorption extends to a few tens of $\mathrm{km\,s^{-1}}$ at maximum into both line wings (Kislyakova et al. 2014; Khodachenko et al. 2017). In the particular case of GJ 9827, the interstellar medium absorption is too close to the blue wing to enable detecting planetary absorption at low velocities and in the red wing the observed stellar emission flux may be too weak to allow detecting the planetary absorption, if present, above the noise level.

It has been suggested that for low-mass planets Lyα absorption may probe the presence of large amounts of water in planetary atmospheres; in this case the hydrogen is the result of water dissociation and further dragging of the lighter hydrogen in the upper layers as a result of the stellar high-energy irradiation (e.g., Bourrier et al. 2017). In this case, the hydrogen originating from the atmospheric water vapor may be detectable, but, as described above, the specific configuration of the stellar emission and interstellar medium absorption hamper detecting the planetary absorption feature. Furthermore, a too large amount of water would also hamper the detection of hydrogen at Lyα because of the reduced atmospheric scale height due to the high mean molecular weight (García Muñoz et al. 2020).

It is also possible that absorption is not observed because the planetary atmosphere does not present enough hydrogen to be detectable. In fact, GJ 9827 b has a bulk density of $7.47^{+1.1}_{0.95}\,\mathrm{g\,cm^{-3}}$, thus consistent with a primarily rocky composition (Kosiarek et al. 2020). Such a high average density may exclude the possibility that the planet hosts a primary, hydrogen-dominated atmosphere or an atmosphere holding large quantities of water. This is indeed the most likely explanation for the lack of planetary Lyα absorption. Given the high average density of the planet, the rather old age of the system, and the short orbital separation,

we can expect that the planet has lost its primary, hydrogen-dominated envelope through escape in the first few hundreds of Myrs (e.g., Kubyshkina et al. 2018a,b), developing then a secondary (e.g., CO_2-dominated) atmosphere as a result of magma ocean solidification. If this process happened while the star was still active, it is even possible that the planet has also lost this secondary atmosphere through hydrodynamic escape (Kulikov et al. 2006; Tian 2009; García Muñoz et al. 2020) leaving behind the bare surface exposed to the action of the stellar wind, which may have then led to the formation of a mineral exosphere (e.g., Miguel et al. 2011; Vidotto et al. 2018), not dissimilar from that of Mercury (e.g., Pfleger et al. 2015).

The conclusion that GJ 9827 b has most likely lost its primary hydrogen-dominated envelope is supported also by calculations of the expected planetary mass-loss rate. We employed the stellar distance and relations of Linsky et al. (2014) to estimate the stellar high-energy emission (X-ray and EUV; hereafter XUV) from the reconstructed Lyα flux, obtaining an XUV flux at 1 AU of $13.01\,\mathrm{erg\,cm^{-2}\,s^{-1}}$. We further inserted the XUV flux, scaled to the distance of planet b, and the system parameters given by Kosiarek et al. (2020) in the "hydro-based approximation" presented by Kubyshkina et al. (2018c) that enables one to analytically derive hydrogen atmospheric mass-loss rates for planets below $40\,M_\oplus$ accounting for all effects included in the hydrodynamic modelling (both core-powered mass-loss and photoevaporation). For GJ 9827 b, we obtained a mass-loss rate of $3.6\times10^{11}\,\mathrm{g\,s^{-1}}$, that is about $1.9\,M_\oplus\,\mathrm{Gyr^{-1}}$ (or about 0.4 planetary masses per Gyr). Considering that the star is $\approx10\,\mathrm{Gyr}$ old (certainly older than 5 Gyr; Rice et al. 2019) and that the star was more active in the past, it is safe to conclude that the planet has lost its primary hydrogen-dominated atmosphere. This is further supported by the rather small restricted Jeans escape parameter Λ (Fossati et al. 2017) of about 20.6, which alone indicates that the planet is subject to intense mass loss, partially driven by the high atmospheric temperature and low planetary gravity (i.e., core powered mass loss).

We followed the same procedure to estimate the atmospheric hydrogen mass-loss rates of GJ 9827 c and GJ 9827 d obtaining $1.0\times10^{11}\,\mathrm{g\,s^{-1}}$ and $5.1\times10^{10}\,\mathrm{g\,s^{-1}}$, respectively. We remark that for all three planets, the mass-loss rates obtained from the hydro-based approximation are within a factor of five from those obtained from directly interpolating the grid of hydrodynamic upper atmosphere models presented by Kubyshkina et al. (2018b). These values correspond to about $0.5\,M_\oplus\,\mathrm{Gyr^{-1}}$ (or about 0.3 planetary masses per Gyr) for GJ 9827 c and about $0.3\,M_\oplus\,\mathrm{Gyr^{-1}}$ (or 0.1 planetary masses per Gyr) for GJ 9827 d. These values and the bulk density of GJ 9827 c ($6.1\,\mathrm{g\,cm^{-3}}$) indicate that it is very unlikely the planet still holds part of its primary hydrogen-dominated at-

mosphere. It is therefore possible that GJ 9827 c has followed an evolutionary path similar to that of GJ 9827 b.

For GJ 9827 d, the lower bulk density of 2.51 g cm^{-3} suggests that the planet may still host part of its primary atmosphere. This may be possible given that the planet appears to have a more sustainable mass-loss rate, suggesting that for this planet mass loss is primarily driven by atmospheric heating due to absorption of the stellar XUV emission, which is in general weaker than core-powered mass loss. However, the large difference between the mass-loss rates we obtained assuming a pure hydrogen atmosphere and those obtained from the constraint given by the non-detection of neutral He in the planetary transmission spectrum ($< 4.2 \times 10^8$ g s^{-1}; Kasper et al. 2020) suggest that the planetary atmosphere may not be hydrogen-dominated. For GJ 9827 d, mass loss is driven by the stellar high-energy emission and therefore its estimate directly depend on it. However a ten times lower stellar XUV emission compared to what is derived from the Lyα flux would bring the planetary mass-loss rate closer to the upper limit given by Kasper et al. (2020). Such lower stellar XUV emission would be close to what is indicated by the Mg II h&k resonance lines. In fact, following Linsky et al. (2013, 2014), the measured Mg II h&k emission flux would imply an XUV flux at 1 AU of 5.97 erg cm^{-2} s^{-1} that is almost 3 times lower than what predicted from the Lyα emission flux. Furthermore one has to consider the rather large uncertainties on the employed conversions that make this value consistent with a ten times lower XUV flux. Nevertheless, even a ten times lower XUV flux would still be about ten times higher than what suggested by the non-detection of the He lines.

Interestingly, GJ 9827 d has a bulk density similar to that of π Men c, which also has a predicted hydrogen mass-loss rate of the order of 10^{10} g s^{-1} (Gandolfi et al. 2018; García Muñoz et al. 2020; Shaikhislamov et al. 2020) and for which Lyα transit observations led to a non-detection of the planetary atmosphere (García Muñoz et al. 2020). Transit observations of GJ 9827 d, and of other similar planets such as π Men c, aiming at characterising their atmospheres would be very valuable for understanding the nature of puffy super-Earths (García Muñoz et al. 2020).

6. CONCLUSIONS

In this paper we presented a search for exospheres around two planets orbiting GJ 9827, a K6 bright star discovered to host three super-Earths in 1:3:5 commensurability from the Kepler/K2 mission. We observed GJ 9827 b with *HST* and GJ 9827 b and d with CARMENES during transit in order to characterize their atmospheres via the Lyα, Hα, and He I transitions, and we found no evidence of an extended atmosphere in either of the planets. Theoretical calculations of the mass-loss rate supported our results, predicting escape

rates of 4.3×10^{11} g s^{-1}, 7.2×10^{12} g s^{-1} and 3.3×10^{10} g s^{-1} for GJ 9827 b, c and d, respectively, making them unlikely to still retain their hydrogen-dominated atmosphere.

We also made use of the *HST* spectra in order to characterize GJ 9827's high energy emission, which was used for the above escape rate calculations, and the ISM absorption along its sightline. We reconstructed the intrinsic Lyα and MgII stellar fluxes, necessary because of attenuating H I and Mg II interstellar gas between us and the star, finding $F(\text{Ly}\alpha) = (5.42^{+0.96}_{-0.75}) \times 10^{-13}$ erg cm^{-2} s^{-1} and $F(\text{MgII}) = (5.64 \pm 0.24) \times 10^{-14}$ erg cm^{-2} s^{-1}. We report that GJ 9827 is Doppler-shifted $+30$ km s^{-1} from the velocity frame of the absorbing ISM gas, which results in almost negligible attenuation of the narrow Mg II lines, but dramatic absorption of the broad Lyα line. However, the reconstructed intrinsic Lyα flux is inconsistent with the literature predictions based on its Mg II emission (Wood et al. 2005; Youngblood et al. 2016). Comparing GJ 9827 to other K dwarfs as well as M dwarfs, we found it to have a significantly high Lyα surface flux and a significantly low Mg II surface flux. This could have important implications on the planetary atmospheres in the system as Lyα and Mg II, the two brightest emission lines in GJ 9827's UV spectrum, have a large effect on atmospheric photochemistry, potentially controlling which are the dominant species in the atmosphere. GJ 9827's Lyα and Mg II flux discrepancy also highlights the importance of caution when using UV scaling relations for atmospheric escape calculations or photochemistry calculations. Not acknowledging the natural variability between individual stars could be detrimental to our assumptions about the composition or even presence of exoplanet atmospheres.

As a nearby system of planets transiting a bright star, GJ 9827 is being intensely studied for a variety of reasons. More *HST* STIS UV transit observations are planned for GJ 9827 b, that will allow us to confirm our results presented here and investigate possible variations in the stellar flux. We have also observed transits of all three Super-Earths orbiting GJ 9827 with *Spitzer* (Livingston et al in prep.). These, together with our approved Cycle 1 GO CHEOPS transit observations, will further enhance dynamical constraints via transit timing variations that will provide invaluable measurements in the infrared to complement our *Hubble* observations, as well as facilitate efficient future observations (e.g., with *JWST*) for a system that will be intensely characterized in the years to come.

REFERENCES

Allart, R., Bourrier, V., Lovis, C., et al. 2018, Science, 362, 1384, doi: 10.1126/science.aat5879

Baraffe, I., Chabrier, G., Barman, T. S., et al. 2005, A&A, 436, L47, doi: 10.1051/0004-6361:200500123

Batalha, N. M., Rowe, J. F., Bryson, S. T., et al. 2013, ApJS, 204, 24, doi: 10.1088/0067-0049/204/2/24

Bauer, F. F., Zechmeister, M., & Reiners, A. 2015, A&A, 581, A117, doi: 10.1051/0004-6361/201526462

Birkby, J. L. 2018, arXiv e-prints, arXiv:1806.04617. https://arxiv.org/abs/1806.04617

Borucki, W. J., Koch, D., Basri, G., et al. 2010, Science, 327, 977, doi: 10.1126/science.1185402

Borucki, W. J., Koch, D. G., Basri, G., et al. 2011, ApJ, 736, 19, doi: 10.1088/0004-637X/736/1/19

Bourrier, V., Ehrenreich, D., King, G., et al. 2017, A&A, 597, A26, doi: 10.1051/0004-6361/201629253

Caballero, J. A., Guàrdia, J., López del Fresno, M., et al. 2016, Society of Photo-Optical Instrumentation Engineers (SPIE) Conference Series, Vol. 9910, CARMENES: data flow, 99100E, doi: 10.1117/12.2233574

Casasayas-Barris, N., Pallé, E., Yan, F., et al. 2018, A&A, 616, A151, doi: 10.1051/0004-6361/201832963

—. 2019, A&A, 628, A9, doi: 10.1051/0004-6361/201935623

Cauley, P. W., Redfield, S., Jensen, A. G., et al. 2015, ApJ, 810, 13, doi: 10.1088/0004-637X/810/1/13

Chen, G., Casasayas-Barris, N., Palle, E., et al. 2020, arXiv e-prints, arXiv:2002.08379. https://arxiv.org/abs/2002.08379

dos Santos, L. A., Ehrenreich, D., Bourrier, V., et al. 2020, A&A, 640, A29, doi: 10.1051/0004-6361/202038802

Ehrenreich, D., Bourrier, V., Wheatley, P. J., et al. 2015, Nature, 522, 459, doi: 10.1038/nature14501

Foreman-Mackey, D., Hogg, D. W., Lang, D., & Goodman, J. 2013, PASP, 125, 306, doi: 10.1086/670067

Fossati, L., Erkaev, N. V., Lammer, H., et al. 2017, A&A, 598, A90, doi: 10.1051/0004-6361/201629716

France, K., Loyd, R. O. P., Youngblood, A., et al. 2016, ApJ, 820, 89, doi: 10.3847/0004-637X/820/2/89

Fulton, B. J., Petigura, E. A., Howard, A. W., et al. 2017, AJ, 154, 109, doi: 10.3847/1538-3881/aa80eb

Gandolfi, D., Barragán, O., Livingston, J. H., et al. 2018, A&A, 619, L10, doi: 10.1051/0004-6361/201834289

García Muñoz, A., Youngblood, A., Fossati, L., et al. 2020, ApJL, 888, L21, doi: 10.3847/2041-8213/ab61ff

Gupta, A., & Schlichting, H. E. 2019, MNRAS, 487, 24, doi: 10.1093/mnras/stz1230

Harman, C. E., Schwieterman, E. W., Schottelkotte, J. C., & Kasting, J. F. 2015, ApJ, 812, 137, doi: 10.1088/0004-637X/812/2/137

Jensen, A. G., Redfield, S., Endl, M., et al. 2012, ApJ, 751, 86, doi: 10.1088/0004-637X/751/2/86

Kasper, D., Bean, J. L., Oklopčić, A., et al. 2020, arXiv e-prints, arXiv:2007.12968. https://arxiv.org/abs/2007.12968

Kausch, W., Noll, S., Smette, A., et al. 2015, A&A, 576, A78, doi: 10.1051/0004-6361/201423909

Khodachenko, M. L., Shaikhislamov, I. F., Lammer, H., et al. 2017, ApJ, 847, 126, doi: 10.3847/1538-4357/aa88ad

Kislyakova, K. G., Holmström, M., Lammer, H., Odert, P., & Khodachenko, M. L. 2014, Science, 346, 981, doi: 10.1126/science.1257829

Kosiarek, M. R., Berardo, D. A., Crossfield, I. J. M., et al. 2020, arXiv e-prints, arXiv:2009.03398. https://arxiv.org/abs/2009.03398

Kreidberg, L. 2015, batman: BAsic Transit Model cAlculatioN in Python. http://ascl.net/1510.002

Kubyshkina, D., Lendl, M., Fossati, L., et al. 2018a, A&A, 612, A25, doi: 10.1051/0004-6361/201731816

Kubyshkina, D., Fossati, L., Erkaev, N. V., et al. 2018b, A&A, 619, A151, doi: 10.1051/0004-6361/201833737

—. 2018c, ApJL, 866, L18, doi: 10.3847/2041-8213/aae586

Kulikov, Y. N., Lammer, H., Lichtenegger, H. I. M., et al. 2006, Planet. Space Sci., 54, 1425, doi: 10.1016/j.pss.2006.04.021

Kulow, J. R., France, K., Linsky, J., & Loyd, R. O. P. 2014, ApJ, 786, 132, doi: 10.1088/0004-637X/786/2/132

Linsky, J. 2019, Host Stars and their Effects on Exoplanet Atmospheres, Vol. 955 (Springer), doi: 10.1007/978-3-030-11452-7

Linsky, J. L., Fontenla, J., & France, K. 2014, ApJ, 780, 61, doi: 10.1088/0004-637X/780/1/61

Linsky, J. L., France, K., & Ayres, T. 2013, ApJ, 766, 69, doi: 10.1088/0004-637X/766/2/69

Linsky, J. L., Wood, B. E., Youngblood, A., et al. 2020, ApJ, 902, 3, doi: 10.3847/1538-4357/abb36f

Lopez, E. D., Fortney, J. J., & Miller, N. 2012, ApJ, 761, 59, doi: 10.1088/0004-637X/761/1/59

Loyd, R. O. P., Shkolnik, E. L., Schneider, A. C., et al. 2020, ApJ, 890, 23, doi: 10.3847/1538-4357/ab6605

Luger, R., Barnes, R., Lopez, E., et al. 2015, Astrobiology, 15, 57,
    doi: 10.1089/ast.2014.1215

Madhusudhan, N. 2019, ARA&A, 57, 617,
    doi: 10.1146/annurev-astro-081817-051846

McCann, J., Murray-Clay, R. A., Kratter, K., & Krumholz, M. R.
    2019, ApJ, 873, 89, doi: 10.3847/1538-4357/ab05b8

Miguel, Y., Kaltenegger, L., Fegley, B., & Schaefer, L. 2011,
    ApJL, 742, L19, doi: 10.1088/2041-8205/742/2/L19

Miguel, Y., Kaltenegger, L., Linsky, J. L., & Rugheimer, S. 2015,
    MNRAS, 446, 345, doi: 10.1093/mnras/stu2107

Murray-Clay, R. A., Chiang, E. I., & Murray, N. 2009, ApJ, 693,
    23, doi: 10.1088/0004-637X/693/1/23

Niraula, P., Redfield, S., Dai, F., et al. 2017, AJ, 154, 266,
    doi: 10.3847/1538-3881/aa957c

Nortmann, L., Pallé, E., Salz, M., et al. 2018, Science, 362, 1388,
    doi: 10.1126/science.aat5348

Owen, J. E., & Wu, Y. 2013, ApJ, 775, 105,
    doi: 10.1088/0004-637X/775/2/105

—. 2017, ApJ, 847, 29, doi: 10.3847/1538-4357/aa890a

Palle, E., Nortmann, L., Casasayas-Barris, N., et al. 2020, arXiv
    e-prints, arXiv:2004.12812. https://arxiv.org/abs/2004.12812

Pfleger, M., Lichtenegger, H. I. M., Wurz, P., et al. 2015,
    Planet. Space Sci., 115, 90, doi: 10.1016/j.pss.2015.04.016

Prieto-Arranz, J., Palle, E., Gandolfi, D., et al. 2018, A&A, 618,
    A116, doi: 10.1051/0004-6361/201832872

Quirrenbach, A., Amado, P. J., Caballero, J. A., et al. 2014, in
    Proc. SPIE, Vol. 9147, Ground-based and Airborne
    Instrumentation for Astronomy V, 91471F,
    doi: 10.1117/12.2056453

Quirrenbach, A., Amado, P. J., Ribas, I., et al. 2018, in Society of
    Photo-Optical Instrumentation Engineers (SPIE) Conference
    Series, Vol. 10702, Ground-based and Airborne Instrumentation
    for Astronomy VII, 107020W, doi: 10.1117/12.2313689

Redfield, S., & Linsky, J. L. 2002, ApJS, 139, 439,
    doi: 10.1086/338650

—. 2004, ApJ, 602, 776, doi: 10.1086/381083

—. 2008, ApJ, 673, 283, doi: 10.1086/524002

Rice, K., Malavolta, L., Mayo, A., et al. 2019, MNRAS, 484, 3731,
    doi: 10.1093/mnras/stz130

Rodriguez, J. E., Vanderburg, A., Eastman, J. D., et al. 2018, AJ,
    155, 72, doi: 10.3847/1538-3881/aaa292

Rowe, J. F., Coughlin, J. L., Antoci, V., et al. 2015, ApJS, 217, 16,
    doi: 10.1088/0067-0049/217/1/16

Salz, M., Czesla, S., Schneider, P. C., et al. 2018, A&A, 620, A97,
    doi: 10.1051/0004-6361/201833694

Shaikhislamov, I. F., Fossati, L., Khodachenko, M. L., et al. 2020,
    arXiv e-prints, arXiv:2006.06959.
    https://arxiv.org/abs/2006.06959

Smette, A., Sana, H., Noll, S., et al. 2015, A&A, 576, A77,
    doi: 10.1051/0004-6361/201423932

Spake, J. J., Sing, D. K., Evans, T. M., et al. 2018, Nature, 557, 68,
    doi: 10.1038/s41586-018-0067-5

Teske, J. K., Wang, S., Wolfgang, A., et al. 2018, AJ, 155, 148,
    doi: 10.3847/1538-3881/aaab56

Tian, F. 2009, ApJ, 703, 905, doi: 10.1088/0004-637X/703/1/905

Tian, F., France, K., Linsky, J. L., Mauas, P. J. D., & Vieytes, M. C.
    2014, Earth and Planetary Science Letters, 385, 22,
    doi: 10.1016/j.epsl.2013.10.024

Vidal-Madjar, A., Lecavelier des Etangs, A., Désert, J. M., et al.
    2003, Nature, 422, 143, doi: 10.1038/nature01448

Vidotto, A. A., Lichtenegger, H., Fossati, L., et al. 2018, MNRAS,
    481, 5296, doi: 10.1093/mnras/sty2130

Wood, B. E., Linsky, J. L., Hébrard, G., et al. 2004, ApJ, 609, 838,
    doi: 10.1086/421325

Wood, B. E., Redfield, S., Linsky, J. L., Müller, H.-R., & Zank,
    G. P. 2005, ApJS, 159, 118, doi: 10.1086/430523

Wyttenbach, A., Ehrenreich, D., Lovis, C., Udry, S., & Pepe, F.
    2015, A&A, 577, A62, doi: 10.1051/0004-6361/201525729

Youngblood, A., France, K., Loyd, R. O. P., et al. 2016, ApJ, 824,
    101, doi: 10.3847/0004-637X/824/2/101

Zechmeister, M., Anglada-Escudé, G., & Reiners, A. 2014, A&A,
    561, A59, doi: 10.1051/0004-6361/201322746